chemosensors

Article

Platinum-Functionalized Hierarchically Structured Flower-like Nickel Ferrite Sheets for High-Performance Acetone Sensing

Ziwen Yang [1], Zhen Sun [1], Yuhao Su [1], Caixuan Sun [2], Peishuo Wang [1], Shaobin Yang [1], Xueli Yang [1,*] and Guofeng Pan [1]

[1] Tianjin Key Laboratory of Electronic Materials and Devices, School of Electronics and Information Engineering, Hebei University of Technology, Tianjin 300401, China; 222526@stu.hebut.edu.cn (Z.Y.); 202311901001@stu.hebut.edu.cn (Z.S.); 233913@stu.hebut.edu.cn (Y.S.); 223829@stu.hebut.edu.cn (P.W.); 223949@stu.hebut.edu.cn (S.Y.); pgf@hebut.edu.cn (G.P.)
[2] School of Information Engineering, Tianjin University of Commerce, Tianjin 300134, China; suncaixuan@tjcu.edu.cn
* Correspondence: xlyang@hebut.edu.cn

Abstract

Acetone detection is crucial for non-invasive health monitoring and environmental safety, so there is an urgent demand to develop high-performance gas sensors. Here, platinum (Pt)-functionalized layered flower-like nickel ferrite ($NiFe_2O_4$) sheets were efficiently fabricated via facile hydrothermal synthesis and wet chemical reduction processes. When the Ni/Fe molar ratio is 1:1, the sensing material forms a Ni/NiO/$NiFe_2O_4$ composite, with performance further optimized by tuning Pt loading. At 1.5% Pt mass fraction, the sensor shows a high acetone response (R_g/R_a = 58.33 at 100 ppm), a 100 ppb detection limit, fast response/recovery times (7/245 s at 100 ppm), and excellent selectivity. The enhancement in performance originates from the synergistic effect of the structure and Pt loading: the layered flower-like morphology facilitates gas diffusion and charge transport, while Pt nanoparticles serve as active sites to lower the activation energy of acetone redox reactions. This work presents a novel strategy for designing high-performance volatile organic compound (VOC) sensors by combining hierarchical nanostructured transition metal ferrites with noble metal modifications.

Keywords: Ni/NiO/$NiFe_2O_4$ sensing composites; acetone sensor; Pt sensitization; bimetallic spinel oxides

check for updates

Received: 24 May 2025
Revised: 18 June 2025
Accepted: 23 June 2025
Published: 26 June 2025

Citation: Yang, Z.; Sun, Z.; Su, Y.; Sun, C.; Wang, P.; Yang, S.; Yang, X.; Pan, G. Platinum-Functionalized Hierarchically Structured Flower-like Nickel Ferrite Sheets for High-Performance Acetone Sensing. *Chemosensors* **2025**, *13*, 234. https://doi.org/10.3390/chemosensors13070234

Copyright: © 2025 by the authors. Licensee MDPI, Basel, Switzerland. This article is an open access article distributed under the terms and conditions of the Creative Commons Attribution (CC BY) license (https://creativecommons.org/licenses/by/4.0/).

1. Introduction

As a common VOC, acetone holds significant relevance across multiple domains, especially in non-invasive medical diagnostics and environmental monitoring [1–4]. In the medical field, elevated acetone levels in exhaled breath (>1.8 ppm) are a key biomarker for diabetes [5–8]. In uncontrolled diabetes, impaired glucose metabolism in the body triggers ketosis, leading to increased acetone production [9,10]. Detecting acetone levels in breath can facilitate early identification of diabetes and evaluation of continuous disease management, providing a non-invasive alternative to traditional blood testing methods [11–15]. From an environmental perspective, acetone is commonly employed in sectors like painting, printing, and chemical manufacturing [16,17]. However, the release of acetone into the atmosphere causes air pollution and the formation of secondary pollutants, including ozone [18,19]. Therefore, accurate and sensitive acetone testing is essential to maintain environmental quality and protect public health.

In order to meet the demand for efficient acetone sensing, researchers have explored various methods for detecting acetone, among which metal oxide-based gas sensors, including those derived from SnO_2, ZnO, and TiO_2, have been widely noticed and studied due to their wide bandwidth, tunable surface defects, and relatively low cost [20–23]. However, these single metal oxides often exhibit inadequate sensitivity, limited selectivity, and high working temperature. Nickel ferrite ($NiFe_2O_4$), a p-type metal oxide featuring a spinel crystal structure, has attracted much attention in gas sensing applications in recent years. Its unique crystal structure and tunable electrical properties make it a promising candidate for sensing materials [24,25]. Numerous studies have reported the utilization of $NiFe_2O_4$ for the fabrication of sensing materials. However, pristine $NiFe_2O_4$ still faces challenges in realizing high-performance acetone sensing, such as low response, limited selectivity, high working temperature, etc. [26–28]. Therefore, in recent years, researchers have taken different means to optimize the properties of $NiFe_2O_4$ sensing materials [29–31].

Constructing hierarchical nanostructures and noble metal functionalization have become effective strategies to improve the gas-sensing performance of metal oxides [32]. Hierarchically structured flower-like architectures, characterized by a high specific surface area and interconnected porous frameworks, are capable of enhancing gas diffusion and offering plentiful active sites for gas adsorption [33,34]. Metallic functionalization has emerged as a viable approach to boost the performance of metal oxide-based gas sensors [35–38]. Noble metals like platinum (Pt) exhibit strong catalytic activity, and when Pt is functionalized onto metal oxide surfaces, it can serve as a catalyst to reduce the activation energy for gas-surface reactions and improve sensor response [39–41]. The present study aims to explore the potential of Pt-functionalized hierarchical structured flowers of nickel ferrite sheets for high-performance acetone sensing, to address the limitations of conventional materials, and to provide a new approach for acetone detection.

In this study, we explored the potential of Pt-functionalized p-type layered flower-like structure nickel ferrite sheets for high-performance acetone sensing. The layered flower-like structure has the unique structural advantage of providing a substantial surface area and efficient gas diffusion channels, which provide effective sites for Pt functionalization. The obtained sensing material exhibits high response and selectivity to acetone, fast response/recovery time, and long-term stability. This research presents a novel method for acetone detection promising for non-invasive medical diagnostic and environmental monitoring applications.

2. Experimental Section

2.1. Synthesis of Nickel Ferrite

The synthesis process of the sensing materials was displayed in Figure 1. 1 mmol of $NiCl_2{\cdot}6H_2O$ (0.2377 g) and 1 mmol of $FeCl_3{\cdot}6H_2O$ (0.2703 g) were poured into 40 mL of ethylene glycol (EG) and stirred magnetically for 20 min until completely dissolved. Then 3 g of anhydrous sodium acetate (CH_3COONa) was introduced to create an alkaline environment, and the solution was allowed to stir for 1 h until the solution turned into a homogeneous dark brown mixture. Finally, the mixture was transferred into a 50 mL Teflon-lined stainless steel autoclave and kept at 200 °C for 12 h. The resulting product was washed four times with deionized water and anhydrous ethanol alternately and dried in air to obtain nickel ferrite powder, which was finally annealed in a muffle furnace at 400 °C for 2 h to yield the $NiO/NiFe_2O_4$ heterojunction, named NFO.

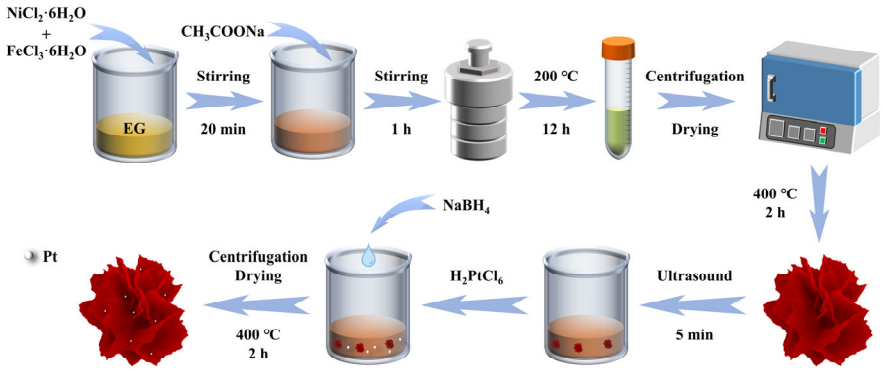


Figure 1. Schematic diagram of the sensing material preparation process.

2.2. Synthesis of Pt-Modified Nickel Ferrite

10 mg of NFO was suspended in 20 mL of deionized water and ultrasonically treated for 5 min to form a uniform dispersion; next, 13.5 μL of H_2PtCl_6 (0.02 g/mL) solution was added dropwise to the mixture, followed by stirring for 10 min. Then 100 μL of $NaBH_4$ (0.1 mmol/mL) was slowly added dropwise, followed by continuous stirring for 3 h. The resultant solution underwent repeated washing with deionized water and anhydrous ethanol in an alternating manner, then air-dried to obtain the powder. Finally, the powder was annealed in a muffle furnace at 400 °C for 2 h to prepare the sensitized nickel ferrite sensing materials with different Pt mass fractions. The 1 wt% Pt-loaded nickel ferrite was named PNFO-1. 1.5 wt% Pt and 2 wt% Pt-loaded sensing materials were obtained using the same preparation method. For 1.5 wt% Pt loading, 20.5 μL of H_2PtCl_6 and 150 μL of $NaBH_4$ were used; for 2 wt% Pt, 27 μL of H_2PtCl_6 and 200 μL of $NaBH_4$ were added. The synthesized samples were named PNFO-1.5 and PNFO-2, respectively. The actual surface atomic ratios obtained through inductively coupled plasma (ICP) analysis are shown in Table S1.

2.3. Characterization

The crystal structure of prepared materials was analyzed by powder X-ray diffraction (XRD, Bruker D8 Discover, Cu-Kα1 radiation source with wavelength 1.5406 Å (Bruker, Billerica, MA, USA)). Morphological features were examined through field emission scanning electron microscopy (FESEM, Zeiss Sigma 500 microscope (Zeiss, Oberkochen, Germany). Microstructural characterization, including transmission electron microscopy (TEM) imaging, high-resolution TEM analysis, and elemental distribution mapping, was performed using a JEOL (JEM2100F) system. Surface chemical composition was determined by X-ray photoelectron spectroscopy (XPS) measurements carried out on an ESCALAB250 spectrometer.

2.4. Gas Sensor Fabrication and Measurement Process

First, the calcined material was mixed into a slurry using an appropriate amount of deionized water and then uniformly coated onto the alumina tube with a brush. A Ni-Cr alloy coil was inserted into the ceramic tube to serve as a heater, generating different operating temperatures through current adjustment. Finally, the two ends of the Ni-Cr alloy coil and the four Pt wires on the alumina tube were soldered to a hexagonal socket to obtain a fabricated sensor, which is shown schematically in Figure S1.

Sensor characterization was conducted in a laboratory environment (25 °C, 30% RH) via a static testing system, which was composed of a Fluke 8864A multimeter and a constant-current power supply (GWinstek, GPD-3303S). The sensors were alternately exposed to a glass vessel containing fresh air and a test gas, and the resistances R_a and R_g were recorded by a Fluke 8864A multimeter, respectively. Regarding reducing gas species, sensor response

magnitude (S) was quantified using the resistance ratio R_g/R_a for p-type sensing materials. Response dynamics were characterized by measuring the temporal intervals required for 90% resistance variation during gas exposure (response phase) and subsequent air recovery (recovery phase). An amount of target gas was introduced into a glass vessel via a microsyringe to achieve a desired concentration for measurement. The VOC gas concentration was calculated as Equation (1):

$$C = \frac{\varphi \times \rho \times V_1 \times 1000 \times R \times T}{M \times V_2 \times P} \quad (1)$$

The gas concentration calculation incorporates the following parameters: C (ppm) corresponds to the target gas concentration; φ (purity), ρ (g/cm^3, density), and V_1 (μL, injection volume) characterize the analyte properties. System parameters include V_2 (L, test chamber volume), M (g/mol, analyte's molecular weight), and the ideal gas constant R (0.082 L·atm·mol^{-1}·K^{-1}). Environmental controls comprised T (298 K, laboratory temperature) and P (1 atm, ambient atmospheric pressure). For sensor humidity testing, a high-low temperature humidity chamber (BPGHJS-100A) served as the humidifier to precisely regulate humidity under a constant laboratory temperature of 25 °C.

3. Results and Discussion

3.1. Material Characterization

XRD spectra of nickel ferrite and nickel ferrite samples with different Pt concentrations were analyzed to explore the crystalline structure of the sensing material. As depicted in Figure 2, all samples showed characteristic diffraction peaks of $NiFe_2O_4$ (PDF#10-0325), confirming the formation of $NiFe_2O_4$. In addition, peaks for NiO (PDF#47-1049) and Ni monomer (PDF#87-0712) were also identified. The characteristic peaks of $NiFe_2O_4$ are still dominant in the XRD spectra of PNFO-1, PNFO-1.5, and PNFO-2, indicating that the introduction of Pt did not damage the crystal structure of $NiFe_2O_4$. In addition, no characteristic peaks of Pt were detected, potentially attributable to the low Pt content and the limited detection precision of the XRD equipment. The simultaneous appearance of peaks of NiO and Ni in all samples is attributed to the 1:1 molar ratio between Ni and Fe during synthesis, and the excess source of Ni generated NiO after the generation of $NiFe_2O_4$, while some Ni ions were reduced to Ni metal by the reduction in EG during the synthesis.

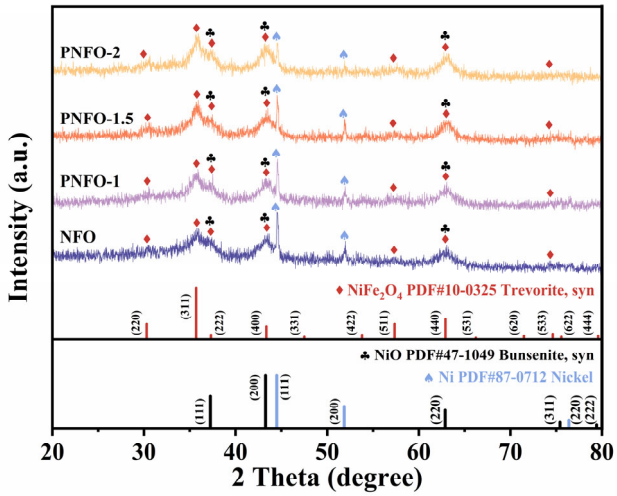


Figure 2. XRD patterns of NFO, PNFO-1, PNFO-1.5, and PNFO-2.

SEM images of the samples are depicted in Figure 3. Figure 3a,b illustrate the morphology of the pristine nickel ferrite sample, which is structured by nanosheets. The rough surface of the prepared sample is observable in the amplified SEM Figure 3b. Figure 3c–h show the SEM images of the Pt-sensitized nickel ferrite samples. The samples all show a flower-like sheet morphology, which indicates that the Pt loading had almost no impact on the initial morphology of the samples. The high-magnification images (Figure 3b,d,f,h) further show that the sheets are thin with irregular edges, which might facilitate the increase in specific surface area. This property is beneficial for gas sensing because the interlaced sheet structure enhances gas adsorption and diffusion, providing a good basis for improving the performance of the material.

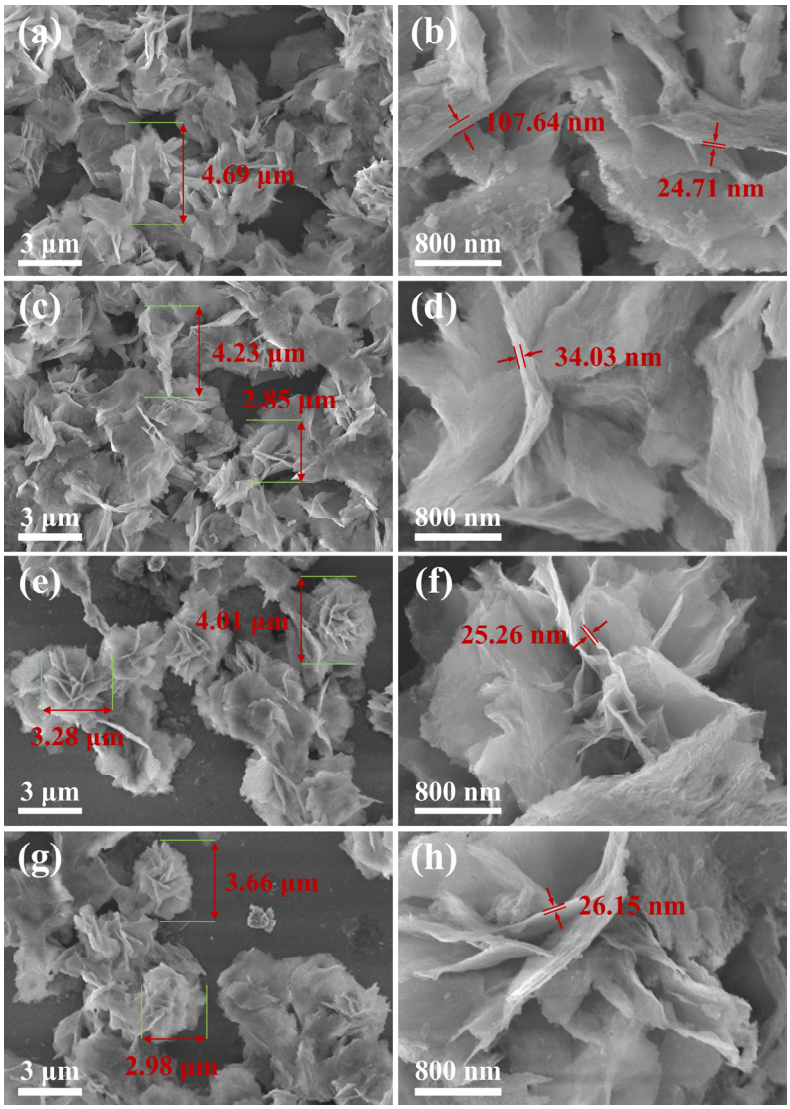


Figure 3. SEM images of NFO (**a**,**b**), PNFO-1 (**c**,**d**), PNFO-1.5 (**e**,**f**), and PNFO-2 (**g**,**h**).

The microstructure and elemental composition of the PNFO-1.5 sample are depicted in detail in Figure 4. The low-magnification TEM image (Figure 4a) reveals that the nanosheets composing the sample are composed of many nanoparticles and have a porous structure. The lattice spacing of 0.251 and 0.318 nm observed in Figure 4b correspond to the (311) crystal plane of $NiFe_2O_4$ and the (111) crystal plane of PtO_2, respectively [5,42]. The lattice spacing of 0.202 nm and 0.241 nm in Figure 4c correspond to the (111) crystallographic plane of Ni and NiO, respectively, indicating that Ni and NiO present simultaneously within the sample [26]. In addition, the Pt (111) crystallographic plane was observed (lattice spacing

of 0.225 nm) [43]. The elemental distribution images of the nanosheets (Figure 4d,e) reveal a homogeneous distribution of Ni, Fe, O, and Pt without obvious agglomeration, indicating that Pt is well dispersed in the samples. This uniform dispersion promotes an increase in active sites within the sensing material and aids in enhancing its gas-sensing performance. And the surface atomic ratios obtained through energy dispersive spectroscopy (EDS) analysis are shown in Table S2. In addition, the selected area electron diffraction (SAED) pattern (Figure 4f) shows typical polycrystalline rings, indicating that the sample has a polycrystalline structure and good crystallinity.

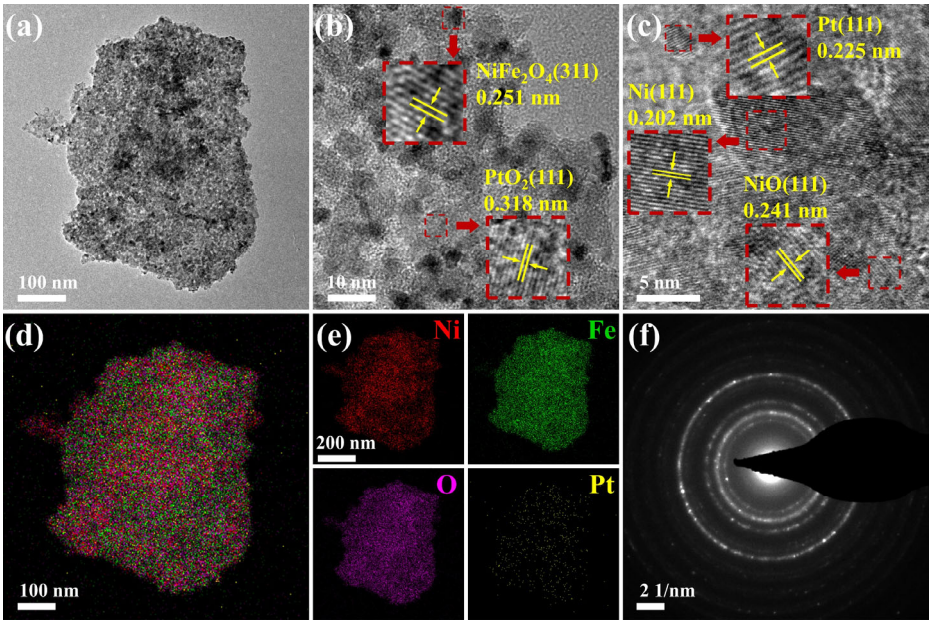


Figure 4. (**a**) TEM image of PNFO-1.5; (**b**,**c**) HRTEM images of PNFO-1.5; (**d**,**e**) EDS mapping images of PNFO-1.5; (**f**) SAED image of PNFO-1.5.

The XPS results for NFO and PNFO-1.5 are demonstrated in Figure 5. The full spectra of both samples are graphically presented in Figure 5a. Both NFO and PNFO-1.5 exhibit characteristic peaks for Ni, Fe, O and C. PNFO-1.5 shows an additional peak for Pt (Pt 4f), confirming the successful loading of Pt. The appearance of carbon characteristic peaks in the samples may be attributed to multiple factors. On the one hand, sodium acetate, as an additive involved in the experiment, may serve as a direct pathway for carbon source introduction. On the other hand, during the testing process, the samples are exposed to the air chamber of the instrument, and hydrocarbons in the air will be adsorbed on the surface of the samples, thereby leading to the generation of carbon signals [44]. For the Ni 2p spectrum (Figure 5b), the peaks at 854.51 and 855.74 eV in NFO belong to Ni^{2+} and Ni^{3+} respectively. In PNFO -1.5, the peak positions are slightly shifted, indicating a change in the chemical environment of Ni owing to Pt functionalization [45,46]. The Fe 2p spectrum (Figure 5c) shows peaks of Fe^{2+} and Fe^{3+} at 710.31 and 711.99 eV. The Fe 2p peaks in NFO and PNFO-1.5, with the slight shifts and intensity changes in NFO and PNFO-1.5, indicate that the electronic structure of the Fe species is also altered by the interaction of Pt [46,47]. Figure 5d shows the Pt 4f spectrum of PNFO-1.5, with peaks at 71.02 and 67.27 eV assigned to Pt^0, which, in conjunction with the peak area ratios presented in the figure, suggests that Pt exists predominantly in the metallic state. In addition, the peaks of 73.79 and 68.74 eV were attributed to Pt^{4+}, implying that some of the Pt was oxidized to PtO_2 during annealing, evidencing that Pt exists as Pt/PtO_2, which synergistically sensitizes the sensing material [43,48–50]. The O 1s spectrum (Figure 5e) was fitted to three components: the O_C (surface adsorbed oxygen), the O_V (oxygen vacancy), and the O_L (lattice oxygen). Figure 5f

shows the proportion of each oxygen species. The higher proportion of O_V (54.36%) for PNFO-1.5 compared to NFO (44.16%) suggests that Pt functionalization increases the amount of oxygen vacancies. Additionally, photoluminescence (PL) measurements (Figure S2) also demonstrated that the O_V concentration of PNFO-1.5 was significantly higher than that of other materials [51–54]. The reason for the elevated O_V may be related to the Pt loading. On the one hand, it is attributed to the lattice constant mismatch at the interface between Pt/PtO_2 and NFO and the disordered arrangement of the atoms at the interface, forming defects, which reduces the binding energy of the oxygen atoms and contributes to the enrichment of oxygen vacancies near the interface. On the other hand, in the course of high-temperature annealing, the diffusion of atoms at the interface between Pt/PtO_2 and NFO is intensified, and the migration of oxygen atoms is enhanced in the process of lattice reconstruction, which makes it easy to form oxygen vacancies [55–58]. These oxygen vacancies can be the active sites for gas adsorption and improve the gas-sensing performance.

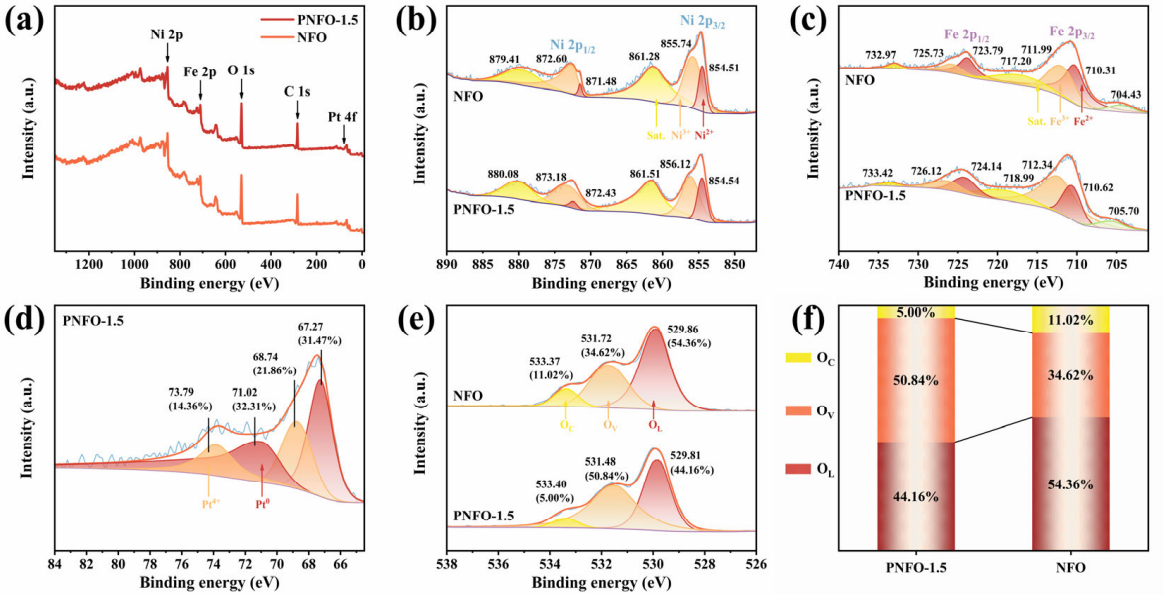


Figure 5. (**a**) XPS survey spectra of the NFO and PNFO-1.5 samples; High-resolution spectra of (**b**) Ni 2p, (**c**) Fe 2p, (**d**) Pt 4f, and (**e**) O 1 s; (**f**) The percentage of the different oxygen species of NFO and PNFO-1.5.

3.2. Gas Sensing Properties

Figure 6 and Figure S3 illustrate the gas-sensing performance of NFO and PNFO sensing materials. Figure 6a-d show the response of NFO, PNFO-1, PNFO-1.5, and PNFO-2 based sensors to various gases (toluene, n-butyl alcohol, methanol, acetone, triethylamine, n-amyl alcohol, trimethylamine, and ammonia) at 100 ppm under various working temperatures. Clearly, the Pt-loaded sensing material exhibits a significantly higher response to acetone than the pristine NFO. The operating temperature was reduced by 50 °C from the pristine 250 °C to 200 °C. This can be attributed to the remarkable catalytic activity of Pt, which significantly lowers the activation energy for the redox reactions of gas molecules at the sensor surface. In addition, it can be noticed that the selectivity of the original NFO sensing material is very poor, whereas Pt modification remarkably enhances the sensor's selectivity. Figure 6e specifically compares the responses of the four sensors to 100 ppm acetone across varying temperatures. Specifically, the response of NFO to acetone at 250 °C is 17.43, while the responses of PNFO-1, PNFO-1.5, and PNFO-2 to acetone at 200 °C are 33.87, 58.33, and 28.12, respectively. The highest response is obtained for PNFO-1.5.

This is due to the fact that the appropriate amount of Pt loading can increase the active sites and oxygen vacancies at the sensing material surface. When Pt is excessively loaded, particle agglomeration occurs, which reduces the interfacial contact between Pt and the sensing material and even covers the active sites at the sensing material surface, leading to a reduction in the gas-sensing performance of the sensor. Figure 6f depicts the variation in the resistance of the sensors as a function of temperature. The high resistance of the pristine NFO and the reduced resistance of the sensor after Pt loading can be ascribed to the increased oxygen vacancy. The increased oxygen vacancies cause more adsorbed oxygen to adsorb at the sensing material surface, capturing electrons in the conduction band, leading to an increase in the number of holes, enhanced conductivity, and reduced resistance of the sensing material.

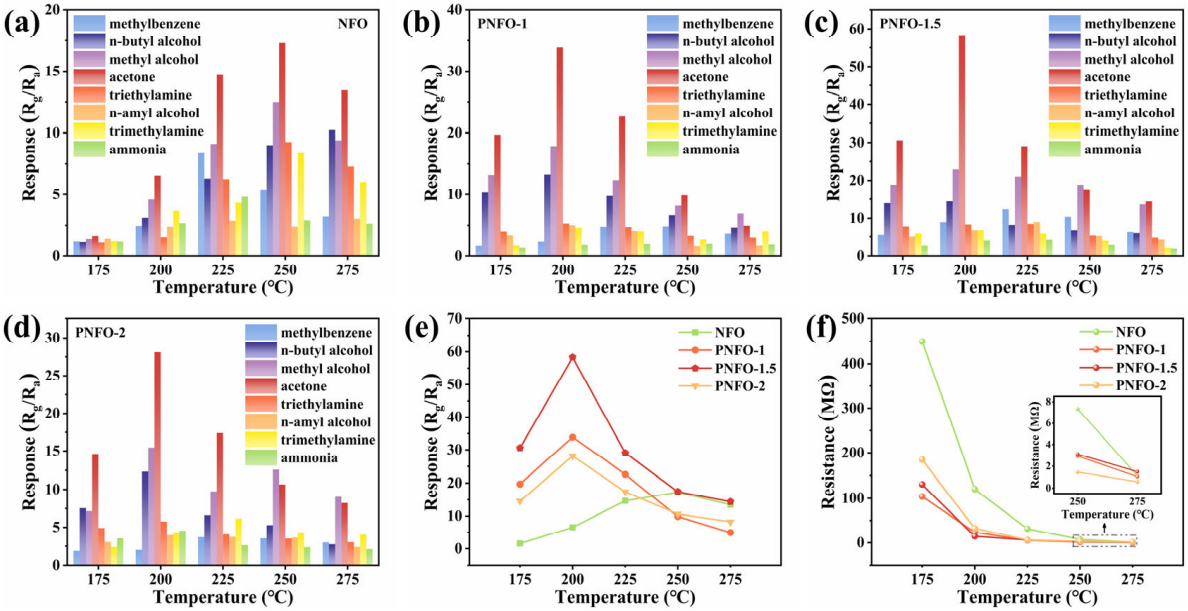


Figure 6. (**a**–**d**) Response of NFO, PNFO-1, PNFO-1.5, and PNFO-2 in 100 ppm gas at different temperatures; (**e**) Temperature-dependent response of the samples to 100 ppm acetone; (**f**) Dynamic resistance change of the gas sensors in air (R_a) at 175–275 °C.

Figure 7 further examines the gas-sensing characteristics of NFO and PNFO sensing materials in different concentrations of acetone gas. Figure 7a–d shows the resistance-time curves of NFO, PNFO-1, PNFO-1.5, and PNFO-2 when exposed to different concentrations of acetone gas. It is clear that the resistance of the sensors increases significantly as the concentration of acetone increases, exhibiting the characteristics of a p-type semiconductor. The dynamic resistance curves depicting the response of the sensor to acetone at lower concentration levels (0.1–3 ppm) are plotted in the insets of Figure 7a–d. It is evident that the four sensors show obvious response fluctuations to 0.1 ppm acetone.

Figure 7e shows the response linearity of the four sensors as a function of acetone concentration. The PNFO samples, especially the PNFO-1.5, showed a higher response compared to the NFO and did not saturate at an acetone concentration of 100 ppm, indicating that the sensors have a wider detection range. Figure 7f and g compare the repeatability and response/recovery characteristics for the NFO and PNFO-1.5 sensors. The repeatability of the two sensors is good, featuring response/recovery times of 6/209 s and 7/245 s for the NFO and PNFO-1.5 sensors, respectively. Figure 7h is an illustration of the stability of the PNFO-1.5 over a period of 30 days, with minimal degradation of the response, suggesting that the sensors exhibit excellent long-term stability. Figure 7i and Figure S4 examine the impact of humidity on the PNFO-1.5 sensor. As humidity increases, the resistance of the

PNFO-1.5 decreases in acetone gas and increases in air. The response of the sensor shows an overall decreasing trend; however, it can be observed that at a humidity of 60% RH, the response of the sensor degrades by less than 20%, indicating acceptable resistance to humidity disturbances.

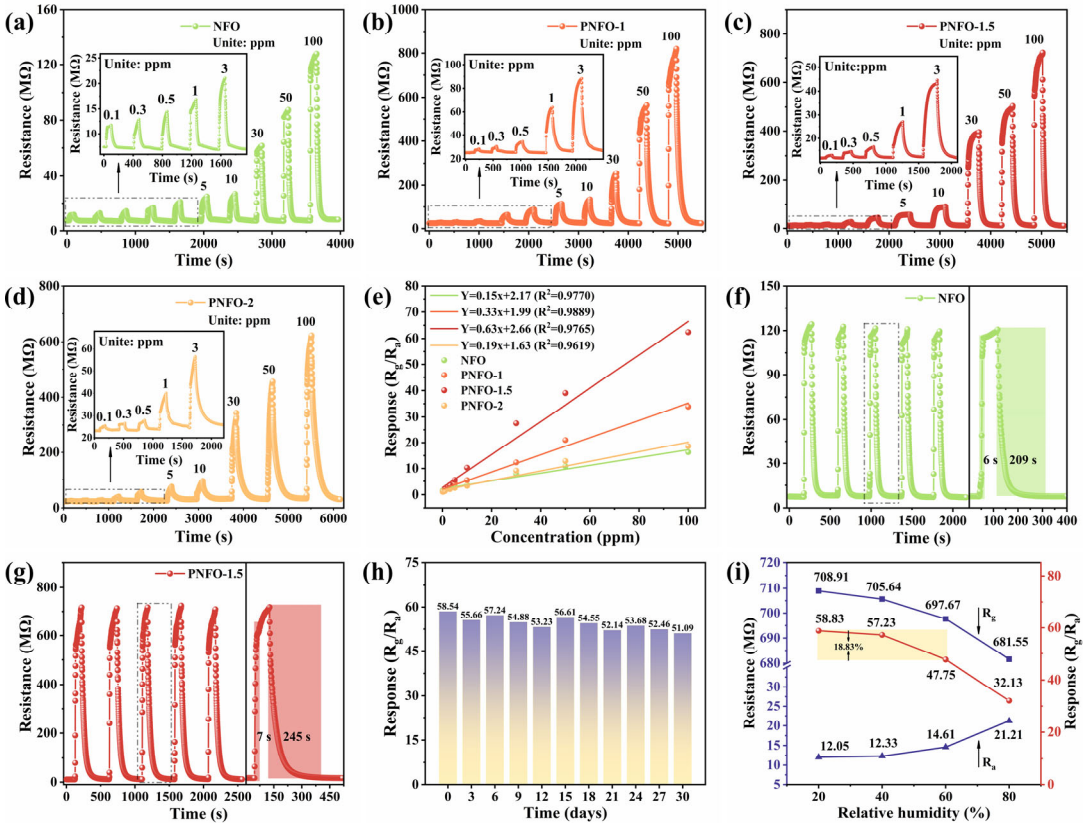


Figure 7. (**a**–**d**) Resistance-time curves of the four sensors to acetone at low (0.1–3 ppm) and high (5–100 ppm) concentrations at their OWT (NFO (250 °C), PNFO-1 (200 °C), PNFO-1.5 (200 °C), PNFO-2 (200 °C)); (**e**) Linear plots between the response of the four gas sensors and the varying concentrations of acetone; (**f**,**g**) Continuous dynamic resistance and response/recovery time recordings of NFO (250 °C) and PNFO-1.5 (200 °C) for 100 ppm acetone; (**h**) Thirty-day response of PNFO-1.5 to 100 ppm acetone; (**i**) Resistance and response of PNFO-1.5 with increasing humidity.

Table 1 presents the gas-sensing performance of Pt-loaded, nickel oxide-based, and nickel ferrite-based acetone gas sensors [27,31,59–70]. From the comparison, it is evident that the gas sensor based on PNFO-1.5 possesses a lower operating temperature and higher gas response, demonstrating its great development potential in the field of acetone sensing.

Table 1. Comparison of gas sensing performance of PNFO-1.5 in this work and other Pt-loaded, nickel oxide-based, and nickel ferrite-based acetone gas sensors.

Materials	Working Temperature (°C)	Concentration (ppm)	Response (R_a/R_g or R_g/R_a)	Response/Recovery Time (s)	Selectivity	Platinum Loading Mass Fraction (wt %)	Ref.
Pt-$BiVO_4$	300	100	12.5 (R_a/R_g)	2/61	2.33	0.476	[59]
Pt-TiO_2	260	200	42.5 (R_a/R_g)	8/11	1.93	2.03	[60]
Pt-ZnO-In_2O_3	300	100	57.1 (R_a/R_g)	1/44	1.89	— —	[61]
Pt-α-Fe_2O_3	220	100	27.2 (R_a/R_g)	1/46	1.7	0.611	[62]
5 wt % Pt/NFO	180	100	221 (R_a/R_g)	12/13	5.45	5	[31]
NiO-WO_3	375	100	22.5 (R_a/R_g)	6/11	2.5	— —	[63]
GO-SnO_2-NiO	350	100	33.5 (R_a/R_g)	4/130	— —	— —	[64]
NiO-Zn_2SnO_4	300	100	49.8 (R_a/R_g)	1/60	2.2	— —	[65]

Table 1. *Cont.*

Materials	Working Temperature (°C)	Concentration (ppm)	Response (R_a/R_g or R_g/R_a)	Response/Recovery Time (s)	Selectivity	Platinum Loading Mass Fraction (wt %)	Ref.
ZnS-NiO	225	50	36 (R_g/R_a)	26.31/16.7	1.5	— —	[66]
$NiFe_2O_4$ core-shell spheres	280	100	10.6 (R_g/R_a)	1/7	3.03	— —	[67]
$NiO/NiFe_2O_4$-1.5	200	100	19.9 (R_g/R_a)	2.4/19.6	1.54	— —	[27]
$NiFe_2O_4$-NiO composites	280	50	23 (R_g/R_a)	— —	1.28	— —	[68]
NiO/NFO-A	170	50	45 (R_g/R_a)	55/261	1.91	— —	[69]
$NiO/NiFe_2O_4$ nanocubes	170	100	150.3 (R_g/R_a)	12.8/15.6	1.17	— —	[70]
PNFO-1.5	200	100	58.33 ± 1.13 (R_g/R_a)	7/245	2.56	1.5	This work

3.3. Gas Sensing Mechanism

As is widely recognized, the sensing mechanism of metal-oxide-semiconductor gas sensors relies on the adsorption and desorption of gas molecules at the surface of the sensing material, along with the surface resistance variation resulting from the redox reaction of test gas molecules on the material surface, as depicted in Figure 8. When the sensor is exposed to air, dissociative adsorption of oxygen molecules occurs at the surface of the sensing material, accompanied by electron transfer from the material's conduction band to form surface chemisorbed oxygen ions (Equations (2)–(4)) [38,71–75]. In the p-type semiconductor sensing material, with holes serving as the majority carriers, exposure to air depletes conduction band electrons and induces the formation of a hole accumulation layer at the surface [76,77]. When the sensor is exposed to acetone gas, surface-adsorbed oxygen ions on the sensing material undergo a redox reaction with acetone gas molecules, Equation (5). During this process, electrons revert to the conduction band of the sensing material, which attenuates the surface hole accumulation layer and correspondingly elevates sensor resistance under reducing gas exposure.

$$O_{2(gas)} \rightarrow O_{2(ads)}, \quad (2)$$

$$O_{2(ads)} + e^- \rightarrow {O_2}^-_{(ads)} \ (<100\ ^\circ C), \quad (3)$$

$${O_2}^-_{(ads)} + e^- \rightarrow 2{O}^-_{(ads)} \ (100-300\ ^\circ C), \quad (4)$$

$$CH_3COCH_3 + 8O^- \rightarrow 3CO_2 + 3H_2O + 8e^- \quad (5)$$

SEM images have shown that both pristine and Pt-loaded nickel ferrite samples exhibit a hierarchical flower-like architecture composed of ultrathin nanosheets with irregular edges. This unique morphology leads to an increased specific surface area, thereby improving the adsorption and diffusion efficiency of oxygen and acetone molecules and, which in turn promotes the progression of the processes described in Equations (2)–(5). The enhanced sensor performance following Pt loading is ascribed to two primary mechanisms: On the one hand, Pt incorporation enhances oxygen vacancy density at the sensing material surface, thereby increasing active site population, which facilitates the adsorption of both oxygen and acetone molecules onto the material surface [74]. This leads to the sensing material exhibiting lower resistance in air, while in acetone gas, the increased participation of acetone molecules in redox reactions results in higher sensor resistance within the acetone environment. On the other hand, Pt has high catalytic activity, accelerates the dissociation and oxidation reaction of acetone, reduces the reaction activation energy, facilitates greater participation of acetone molecules in the reaction, releases more electrons, and makes the response of the sensor more significant [78–81].

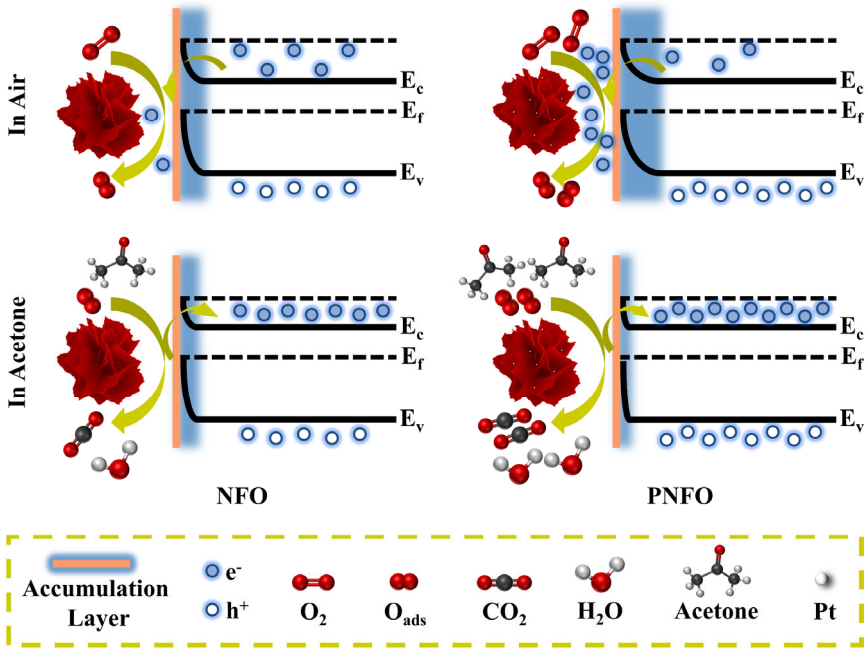


Figure 8. Schematic sensing mechanism of the sensor.

Finally, it should also be noted that the presence of metallic Ni may also affect the performance of the sensor. Ni accelerates carrier migration [82] and can introduce defects such as oxygen vacancies in metal oxides, which can serve as adsorption sites for gas molecules and improve the sensitivity of the sensor [83,84].

4. Conclusions

In conclusion, Pt/PtO_2-modified nickel ferrite (NFO) flower-like nanosheet materials for acetone gas sensing applications were successfully prepared in this research. Characterization techniques, such as TEM, HRTEM, XPS, and SAED, confirmed that the Pt/PtO_2 and NFO formed a composite structure. XPS analysis showed that Pt functionalization increased the oxygen vacancy content in NFO, which is essential for gas adsorption. Gas-sensing performance tests showed that the Pt-modified NFO samples had superior acetone-sensing characteristics relative to pristine NFO. Specifically, the PNFO-1.5 sample showed the greatest response to acetone, registering a response value of 58.33 at 200 °C for 100 ppm acetone, while the sensor displayed excellent repeatability, response/recovery characteristics, and long-term stability. Owing to the catalytic activity of Pt and the increase in oxygen vacancies at the sensing material surface, the gas adsorption was enhanced while the operating temperature was reduced, which improved the sensor's overall performance. The results of this study demonstrate the potential of Pt/PtO_2-sensitized nickel ferrite composites as high-performance gas-sensing materials for acetone detection applications.

Supplementary Materials: The following supporting information can be downloaded at: https://www.mdpi.com/article/10.3390/chemosensors13070234/s1, Figure S1: Schematic Diagram of Sensor Device; Figure S2: Photoluminescence spectra of NFO, PNFO-1, PNFO-1.5, and PNFO-2 after an excitation at 400 nm; Figure S3: Selectivity Test of NFO, PNFO-1, PNFO-1.5, and PNFO-2 at their OWT (NFO (250 °C), PNFO-1 (200 °C), PNFO-1.5 (200 °C), PNFO-2 (200 °C)); Figure S4: Dynamic resistance response curves of PNFO-1.5 to 100 ppm acetone at 200 °C under (a) 20% RH, (b) 40% RH, (c) 60% RH, and (d) 80% RH; Table S1: The surface atomic ratios obtained through ICP analysis; Table S2: The surface atomic ratios obtained through EDS analysis.

Author Contributions: Conceptualization, X.Y. and Z.Y.; methodology, X.Y. and Z.S.; formal analysis, Z.Y.; investigation, Z.S., Y.S., C.S., P.W., and S.Y.; data curation, Z.Y.; writing—original draft preparation, Z.Y.; writing—review and editing, X.Y., and G.P.; supervision, X.Y., and G.P.; funding acquisition, X.Y. and G.P. All authors have read and agreed to the published version of the manuscript.

Funding: This research was funded by National Natural Science Foundation of China (No. 62473126, 62003123). Hebei Collaborative Innovation Center of Microelectronic Materials and Technology on Ultra Precision Processing (CIC) and Hebei Engineering Research Center of Microelectronic Materials and Devices (ERC).

Institutional Review Board Statement: Not applicable.

Informed Consent Statement: Not applicable.

Data Availability Statement: The original contributions presented in this study are included in the article. Further inquiries can be directed to the corresponding author.

Conflicts of Interest: The authors declare no conflicts of interest.

References

1. Mathur, M.; Verma, A.; Singh, A.; Yadav, B.C.; Chaudhary, V. $CuMoO_4$ nanorods-based acetone chemiresistor-enabled non-invasive breathomic-diagnosis of human diabetes and environmental monitoring. *Environ. Res.* **2023**, *229*, 115931. [CrossRef] [PubMed]
2. Roy, N.; Sinha, R.; Nemade, H.B.; Mandal, T.K. Synthesis of MoS_2-CuO nanocomposite for room temperature acetone sensing application. *J. Alloys Compd.* **2022**, *910*, 164891. [CrossRef]
3. Zhang, H.; Xiao, J.; Chen, J.; Zhang, L.; Zhang, Y.; Pei, X.L. Pd-modified $SmFeO_3$ with hollow tubular structure under light shows extremely high acetone gas sensitivity. *Rare Met.* **2023**, *42*, 545–557. [CrossRef]
4. Li, Z.; Li, S.; Song, Z.; Yang, X.; Wang, Z.; Zhang, H.; Guo, L.; Sun, C.; Liu, H.; Shao, J.; et al. Influence of nickel doping on ultrahigh toluene sensing performance of core-shell ZnO microsphere gas sensor. *Chemosensors* **2022**, *10*, 327. [CrossRef]
5. Zhang, S.F.; Jiang, W.H.; Li, Y.W.; Yang, X.L.; Sun, P.; Liu, F.M.; Yan, X.; Gao, Y.; Liang, X.H.; Ma, J.; et al. Highly-sensitivity acetone sensors based on spinel-type oxide ($NiFe_2O_4$) through optimization of porous structure. *Sens. Actuators B-Chem.* **2019**, *291*, 266–274. [CrossRef]
6. Ama, O.; Sadiq, M.; Johnson, M.; Zhang, Q.; Wang, D. Novel 1D/2D KWO/$Ti_3C_2T_x$ nanocomposite-based acetone sensor for diabetes prevention and monitoring. *Chemosensors* **2020**, *8*, 102. [CrossRef]
7. Sun, J.; Shi, D.; Wang, L.; Yu, X.; Song, B.; Li, W.; Zhu, J.; Yang, Y.; Cao, B.; Jiang, C. CRDS technology-based integrated breath gas detection system for breath acetone real-time accurate detection application. *Chemosensors* **2024**, *12*, 261. [CrossRef]
8. Fan, X.; Yang, S.; Huang, C.; Lu, Y.; Dai, P. Preparation and enhanced acetone-sensing properties of ZIF-8-derived Co_3O_4@ZnO microspheres. *Chemosensors* **2023**, *11*, 376. [CrossRef]
9. Cai, L.B.; Dong, X.Q.; Wu, G.G.; Sun, J.P.; Chen, N.; Wei, H.Z.; Zhu, S.; Tian, Q.Y.; Wang, X.Y.; Jing, Q.; et al. Ultrasensitive acetone gas sensor can distinguish the diabetic state of people and its high performance analysis by first-principles calculation. *Sens. Actuators B-Chem.* **2022**, *351*, 130863. [CrossRef]
10. Arakawa, T.; Mizukoshi, N.; Iitani, K.; Toma, K.; Mitsubayashi, K. A bio-fluorometric acetone gas imaging system for the dynamic analysis of lipid metabolism in human breath. *Chemosensors* **2021**, *9*, 258. [CrossRef]
11. Liu, H.; Liu, W.X.; Sun, C.X.; Huang, W.Z.; Cui, X.L. A review of non-invasive blood glucose monitoring through breath acetone and body surface. *Sens. Actuators A-Phys.* **2024**, *374*, 115500. [CrossRef]
12. Righettoni, M.; Tricoli, A.; Pratsinis, S.E. Si:WO_3 sensors for highly selective detection of acetone for easy diagnosis of diabetes by breath analysis. *Anal. Chem.* **2010**, *82*, 3581–3587. [CrossRef] [PubMed]
13. Hu, J.Y.; Lei, H.; Zhang, H.Y.; Xue, X.X.; Wang, X.P.; Wang, C.H.; Zhang, Y. High reliable gas sensor based on crystal-facet regulated α-Fe_2O_3 nanocrystals for rapid detection of exhaled acetone. *Rare Met.* **2024**, *43*, 6500–6515. [CrossRef]
14. Ueda, T.; Torai, S.; Fujita, K.; Shimizu, Y.; Hyodo, T. Effects of Au addition to porous CuO_2-added SnO_2 gas sensors on their VOC-sensing properties. *Chemosensors* **2024**, *12*, 153. [CrossRef]
15. Muramatsu, Y.; Watanabe, S.; Osada, M.; Tajima, K.; Karashima, A.; Maruo, Y.Y. Small acetone sensor with a porous colorimetric chip for breath acetone detection using the flow–stop method. *Chemosensors* **2025**, *13*, 136. [CrossRef]
16. Koo, A.; Yoo, R.; Woo, S.P.; Lee, H.-S.; Lee, W. Enhanced acetone-sensing properties of Pt-decorated Al-doped ZnO nanoparticles. *Sens. Actuators B Chem.* **2019**, *280*, 109–119. [CrossRef]
17. Maji, B.; Singh, P.; Badhulika, S. A highly sensitive and fully flexible Fe-Co metal-organic framework hydrogel based gas sensor for ppb level detection of acetone. *Appl. Surf. Sci.* **2024**, *678*, 161047. [CrossRef]

18. Wang, S.Y.; Apel, E.C.; Schwantes, R.H.; Bates, K.H.; Jacob, D.J.; Fischer, E.V.; Hornbrook, R.S.; Hills, A.J.; Emmons, L.K.; Pan, L.L.; et al. Global atmospheric budget of acetone: Air-sea exchange and the contribution to hydroxyl radicals. *J. Geophys. Res. Atmos.* **2020**, *125*, e2020JD032553. [CrossRef]
19. Dong, Y.; Du, L.; Jiang, Y.; Wang, Y.; Zhang, J.; Wang, X.; Wei, S.; Sun, M.; Lu, Q.; Yin, G. In_2O_3-SnO_2 hedgehog-like nanostructured heterojunction for acetone detection. *Appl. Surf. Sci.* **2024**, *654*, 159543. [CrossRef]
20. Xing, X.X.; Chen, N.; Yang, Y.; Zhao, R.J.; Wang, Z.Z.; Wang, Z.D.; Zou, T.; Wang, Y.D. Pt-functionalized nanoporous TiO_2 nanoparticles with enhanced gas sensing performances toward acetone. *Phys. Status Solidi A-Appl. Mater. Sci.* **2018**, *215*, 1800100. [CrossRef]
21. Hu, Y.; Wang, H.; Liu, D.; Lin, G.; Wan, J.W.; Jiang, H.; Lai, X.Y.; Hao, S.J.; Liu, X.H. Lychee-like ZnO/$ZnFe_2O_4$ core-shell hollow microsphere for improving acetone gas sensing performance. *Ceram. Int.* **2020**, *46*, 5960–5967. [CrossRef]
22. Wang, Y.; Wei, Z.H.; Li, P.W.; Li, G.; Lian, K.; Zhang, W.D.; Zhuiykov, S.; Hu, J. Pr_6O_{11}-functionalized SnO_2 flower-like architectures for highly efficient, stable, and selective acetone detection. *IEEE Sens. J.* **2018**, *18*, 933–940. [CrossRef]
23. Jin, S.C.; Wu, D.; Song, W.A.; Hao, H.S.; Gao, W.Y.; Yan, S. Superior acetone sensor based on hetero-interface of $SnSe_2$/SnO_2 quasi core shell nanoparticles for previewing diabetes. *J. Colloid Interface Sci.* **2022**, *621*, 119–130. [CrossRef]
24. Narang, S.B.; Pubby, K. Nickel spinel ferrites: A review. *J. Magn. Magn. Mater.* **2021**, *519*, 167163. [CrossRef]
25. Rathore, D.; Kurchania, R.; Pandey, R.K. Nanoferrites gas sensors: A critical review. *Sens. Actuators A-Phys.* **2024**, *379*, 115968. [CrossRef]
26. Ma, Y.; Lu, Y.; Gou, H.; Zhang, W.; Yan, S.; Xu, X. Octahedral $NiFe_2O_4$ for high-performance gas sensor with low working temperature. *Ceram. Int.* **2018**, *44*, 2620–2625. [CrossRef]
27. Yang, J.; Jiang, B.; Wang, X.; Wang, C.; Sun, Y.; Zhang, H.; Shimanoe, K.; Lu, G. MOF-derived porous NiO/$NiFe_2O_4$ nanocubes for improving the acetone detection. *Sens. Actuators B-Chem.* **2022**, *366*, 131985. [CrossRef]
28. Zhang, Y.; Zhou, Y.; Li, Z.; Chen, G.; Mao, Y.; Guan, H.; Dong, C. MOFs-derived $NiFe_2O_4$ fusiformis with highly selective response to xylene. *J. Alloys Compd.* **2019**, *784*, 102–110. [CrossRef]
29. Liao, X.; Liu, X.; Wu, Y.; Qian, L.; Chen, Y.; Wang, Y.; Wu, Z.; Huang, A.; Liu, X.; Luo, J. $Ni_{1-x}Zn_xFe_2O_4$ heterojunction composites derived from normal/inverse spinel structure for ppb-level acetone detection. *Sens. Actuators B-Chem.* **2025**, *436*, 137733. [CrossRef]
30. Fu, Q.; Li, J.; Handschuh-Wang, S.; Zhou, X.; Liu, Y. Synergistic effect of $NiFe_2O_4$ and MWCNTs for ppb-level acetone detection at 150 °C. *Sens. Actuators B-Chem.* **2025**, *425*, 136948. [CrossRef]
31. Xie, J.; Xie, T.; An, C.; Zhao, Y.; Wu, J.; Wu, X. Amorphous Pt-decorated $NiFe_2O_4$ nanorods for acetone sensing. *ACS Appl. Nano Mater.* **2024**, *7*, 28478–28485. [CrossRef]
32. Lv, Y.K.; Yao, B.H.; Liu, Z.Q.; Liang, S.; Liu, Q.C.; Zhai, K.H.; Li, Z.J.; Yao, H.C. Hierarchical Au-loaded WO_3 hollow microspheres with high sensitive and selective properties to toluene and xylene. *IEEE Sens. J.* **2019**, *19*, 5413–5420. [CrossRef]
33. Zhu, L.; Li, Y.Q.; Zeng, W. Hydrothermal synthesis of hierarchical flower-like ZnO nanostructure and its enhanced ethanol gas-sensing properties. *Appl. Surf. Sci.* **2018**, *427*, 281–287. [CrossRef]
34. Wang, Y.H.; Zhang, L.Z.; Zhang, C.S.; Xu, X.M.; Xie, Y.Y.; Chen, W.J.; Wang, J.; Zhang, R.Q. Promoting the generation of active oxygen over Ag-modified nanoflower-like α-MnO_2 for soot oxidation: Experimental and DFT studies. *Ind. Eng. Chem. Res.* **2020**, *59*, 10407–10417. [CrossRef]
35. Kim, T.; Lee, T.H.; Park, S.Y.; Eom, T.H.; Cho, I.; Kim, Y.; Kim, C.; Lee, S.A.; Choi, M.-J.; Suh, J.M.; et al. Drastic gas sensing selectivity in 2-dimensional MoS_2 nanoflakes by noble metal decoration. *ACS Nano* **2023**, *17*, 4404–4413. [CrossRef]
36. Liu, C.; Kuang, Q.; Xie, Z.X.; Zheng, L.S. The effect of noble metal (Au, Pd and Pt) nanoparticles on the gas sensing performance of SnO_2-based sensors: A case study on the {221} high-index faceted SnO_2 octahedra. *Crystengcomm* **2015**, *17*, 6308–6313. [CrossRef]
37. Yin, Y.; Shen, Y.; Zhao, S.; Bai, J.; Qi, Y.; Han, C.; Wei, D. Effect of noble metal elements on ethanol sensing properties of $ZnSnO_3$ nanocubes. *J. Alloys Compd.* **2021**, *887*, 161409. [CrossRef]
38. Gao, D.H.; Yu, Q.C.; Kebeded, M.A.; Zhuang, Y.Y.; Huang, S.; Jiao, M.Z.; He, X.J. Advances in modification of metal and noble metal nanomaterials for metal oxide gas sensors: A review. *Rare Met.* **2025**, *44*, 1443–1496. [CrossRef]
39. Hanh, N.H.; Duy, L.V.; Hung, C.M.; Xuan, C.T.; Duy, N.V.; Hoa, N.D. High-performance acetone gas sensor based on Pt–Zn_2SnO_4 hollow octahedra for diabetic diagnosis. *J. Alloys Compd.* **2021**, *886*, 161284. [CrossRef]
40. Chen, X.; Liu, T.; Ouyang, Y.; Huang, S.; Zhang, Z.; Liu, F.; Qiu, L.; Wang, C.; Lin, X.; Chen, J.; et al. Influence of different Pt functionalization modes on the properties of CuO gas-sensing materials. *Sensors* **2024**, *24*, 120. [CrossRef]
41. Jolly Bose, R.; Illyasukutty, N.; Tan, K.S.; Rawat, R.S.; Vadakke Matham, M.; Kohler, H.; Mahadevan Pillai, V.P. Preparation and characterization of Pt loaded WO_3 films suitable for gas sensing applications. *Appl. Surf. Sci.* **2018**, *440*, 320–330. [CrossRef]
42. Yang, B.X.; Liu, J.Y.; Qin, H.; Liu, Q.; Jing, X.Y.; Zhang, H.Q.; Li, R.M.; Huang, G.Q.; Wang, J. PtO_2-nanoparticles functionalized CuO polyhedrons for n-butanol gas sensor application. *Ceram. Int.* **2018**, *44*, 10426–10432. [CrossRef]
43. Dong, J.Y.; Liu, H.Y.; Sun, C.X.; Shao, J.K.; Wang, M.J.; He, P.; Qi, Y.H.; Pan, G.F.; Yang, X.L. Low-temperature and high-efficient detection of triethylamine based on Pt/PtO_2 loaded WO_3 gas sensors. *J. Alloys Compd.* **2023**, *966*, 171642. [CrossRef]

44. Greczynski, G.; Hultman, L. The same chemical state of carbon gives rise to two peaks in X-ray photoelectron spectroscopy. *Sci. Rep.* **2021**, *11*, 11195. [CrossRef]
45. Tran, P.K.L.; Nguyen, T.H.; Tran, D.T.; Dinh, V.; Ta, T.T.N.; Chung-Li, D.; Kim, N.H.; Lee, J.H. Tunable charge Pt sites-dominated alloy confined by mxene-derived oxycarbide enables ultra-stable ampere-level hydrogen production. *Appl. Catal. B-Environ. Energy* **2025**, *363*, 124801. [CrossRef]
46. Yang, M.Y.; Zhang, J.L.; Zhang, W.Z.Z.; Wu, Z.C.; Gao, F. Pt nanoparticles/Fe-doped α-Ni$(OH)_2$ nanosheets array with low Pt loading as a high-performance electrocatalyst for alkaline hydrogen evolution reaction. *J. Alloys Compd.* **2020**, *823*, 153790. [CrossRef]
47. Zhu, G.H.; Wu, K.; Tan, L.; Wang, W.Y.; Huang, Y.P.; Liu, D.Y.; Yang, Y.Q. Liquid phase conversion of phenols into aromatics over magnetic Pt/NiO-Al_2O_3@Fe_3O_4 catalysts via a coupling process of hydrodeoxygenation and dehydrogenation. *Acs Sustain. Chem. Eng.* **2018**, *6*, 10078–10086. [CrossRef]
48. Sharma, B.; Karuppasamy, K.; Srivastava, A.K.; Alfantazi, A.; Sharma, A. Highly sensitive and selective nanoengineered PtO_2-BNNT heterostructures for ppb level ammonia gas sensing. *Sens. Actuators B-Chem.* **2024**, *400*, 134818. [CrossRef]
49. Xia, Y.; Guo, S.H.; Yang, L.; He, S.F.; Zhou, L.X.; Wang, M.J.; Gao, J.Y.; Hou, M.; Wang, J.; Komarneni, S. Enhanced free-radical generation on MoS_2/Pt by light and water vapor co-activation for selective CO detection with high sensitivity. *Adv. Mater.* **2023**, *35*, 2303523. [CrossRef]
50. Xue, L.X.; Ren, Y.; Li, Y.Y.; Xie, W.H.; Chen, K.Y.; Zou, Y.D.; Wu, L.M.; Deng, Y.H. Pt-Pd nanoalloys functionalized mesoporous SnO_2 spheres: Tailored synthesis, sensing mechanism, and device integration. *Small* **2023**, *19*, 2302327. [CrossRef]
51. Gandhi, A.C.; Wu, S.Y. Strong deep-level-emission photoluminescence in NiO nanoparticles. *Nanomaterials* **2017**, *7*, 231. [CrossRef] [PubMed]
52. Boulahbel, H.; Benamira, M.; Bouremmad, F.; Ahmia, N.; Kiamouche, S.; Lahmar, H.; Souici, A.; Trari, M. Enhanced photodegradation of Congo red dye under sunlight irradiation by p-n $NiFe_2O_4$/TiO_2 heterostructure. *Inorg. Chem. Commun.* **2023**, *154*, 110921. [CrossRef]
53. Mrabet, C.; Jaballah, R.; Mahdhi, N.; Boukhachem, A.; Amlouk, M. Structural, optical, photoluminescence and sunlight photocatalytic properties of sprayed NiO-ZnO nanocomposite thin films. *Mater. Sci. Eng. B-Adv. Funct. Solid-State Mater.* **2024**, *300*, 117130. [CrossRef]
54. Wang, Z.Y.; Miao, J.Y.; Zhang, H.X.; Wang, D.; Sun, J.B. Hollow cubic $ZnSnO_3$ with abundant oxygen vacancies for H_2S gas sensing. *J. Hazard. Mater.* **2020**, *391*, 122226. [CrossRef]
55. Liu, L.B.; Tang, Y.F.; Liu, S.; Yu, M.L.; Sun, Y.F.; Fu, X.Z.; Luo, J.L.; Liu, S.B. Unraveling the trade-off between oxygen vacancy concentration and ordering of perovskite oxides for efficient lattice oxygen evolution. *Adv. Energy Mater.* **2024**, *15*, 2402967. [CrossRef]
56. Huang, N.; Qu, Z.P.; Dong, C.; Qin, Y.; Duan, X.X. Superior performance of α@β-MnO_2 for the toluene oxidation: Active interface and oxygen vacancy. *Appl. Catal. A-Gen.* **2018**, *560*, 195–205. [CrossRef]
57. Jiayu, Z.; Lin, Y.; Zhihao, Z.; Chunran, Z.; Linjiang, F.; Xin, H.; Hongjun, L.; Leihong, Z.; Yiming, H. Preparation of $NaNbO_3$ microcube with abundant oxygen vacancies and its high photocatalytic N_2 fixation activity in the help of Pt nanoparticles. *J. Colloid Interface Sci.* **2023**, *636*, 480–491. [CrossRef]
58. Zhong-Kang, H.; Wen, L.; Yi, G. Advancing the understanding of oxygen vacancies in ceria: Insights into their formation, behavior, and catalytic roles. *JACS Au* **2025**, *5*, 1549–1569. [CrossRef]
59. Xiao, Y.; Hu, S.; Liu, Y.; Zhang, A.; Yao, Z.; Tian, Y.; Li, H.; Ning, Y.; Li, F.; Qu, F.; et al. Pt-modified $BiVO_4$ nanosheets for enhanced acetone sensing. *Sens. Actuators B-Chem.* **2023**, *389*, 133853. [CrossRef]
60. Zhang, K.; Wei, H.; Li, Y.S.; Zhang, W.R.; Zhu, P.D.; Zhang, R.Y. Ultrahigh-acetone-sensitivity sensor based on Pt-loaded TiO_2 porous nanoparticles synthesized via a facile hydrothermal method. *Nanotechnology* **2024**, *35*, 045502. [CrossRef]
61. Guo, L.; Chen, F.; Xie, N.; Kou, X.; Wang, C.; Sun, Y.; Liu, F.; Liang, X.; Gao, Y.; Yan, X.; et al. Ultra-sensitive sensing platform based on Pt-ZnO-In_2O_3 nanofibers for detection of acetone. *Sens. Actuators B-Chem.* **2018**, *272*, 185–194. [CrossRef]
62. Liu, C.; Gao, H.; Wang, L.; Wang, T.; Yang, X.; Sun, P.; Gao, Y.; Liang, X.; Liu, F.; Song, H.; et al. Facile synthesis and the enhanced sensing properties of Pt-loaded α-Fe_2O_3. porous nanospheres. *Sens. Actuators B-Chem.* **2017**, *252*, 1153–1162. [CrossRef]
63. Zhang, J.; Lu, H.; Liu, C.; Chen, C.; Xin, X. Porous NiO-WO_3 heterojunction nanofibers fabricated by electrospinning with enhanced gas sensing properties. *RSC Adv.* **2017**, *7*, 40499–40509. [CrossRef]
64. Jiang, L.; Tu, S.; Xue, K.; Yu, H.; Hou, X. Preparation and gas-sensing performance of GO/SnO_2/NiO gas-sensitive composite materials. *Ceram. Int.* **2021**, *47*, 7528–7538. [CrossRef]
65. Zhou, C.; Meng, F.; Chen, K.; Yang, X.; Wang, T.; Sun, P.; Liu, F.; Yan, X.; Shimanoe, K.; Lu, G. High sensitivity and low detection limit of acetone sensor based on NiO/Zn_2SnO_4 p-n heterojunction octahedrons. *Sens. Actuators B-Chem.* **2021**, *339*, 129912. [CrossRef]
66. Lekshmi, M.S.; Suja, K.J. Enhanced acetone detection using ZnS-NiO heterojunction sensor for diabetes detection. *Ceram. Int.* **2024**, *50*, 23577–23585. [CrossRef]

67. Zhou, T.; Zhang, T.; Zeng, Y.; Zhang, R.; Lou, Z.; Deng, J.; Wang, L. Structure-driven efficient $NiFe_2O_4$ materials for ultra-fast response electronic sensing platform. *Sens. Actuators B-Chem.* **2018**, *255*, 1436–1444. [CrossRef]
68. Xu, Y.; Fan, Y.; Tian, X.; Liang, Q.; Liu, X.; Sun, Y. p-p heterojunction composite of $NiFe_2O_4$ nanoparticles-decorated NiO nanosheets for acetone gas detection. *Mater. Lett.* **2020**, *270*, 127728. [CrossRef]
69. Sun, Y.H.; Huang, Q.T.; Liu, Y.F.; Gu, Z.Q.; Bo, L.B.; Zheng, X.H. Fabrication of NiO nanosheet/$NiFe_2O_4$ nanoparticle sensor through one-step hydrothermal method for acetone detection. *J. Electrochem. Soc.* **2025**, *172*, 017517. [CrossRef]
70. Zhang, D.; Wang, T.T.; Huo, L.H.; Gao, S.; Li, B.S.; Guo, C.Y.; Yu, H.X.; Major, Z.; Zhang, X.F.; Cheng, X.L.; et al. Small size porous NiO/$NiFe_2O_4$ nanocubes derived from Ni-Fe bimetallic metal-organic frameworks for fast volatile organic compounds detection. *Appl. Surf. Sci.* **2023**, *623*, 157075. [CrossRef]
71. Wang, P.; Guo, S.S.; Zhao, Y.N.; Hu, Z.X.; Tang, Y.T.; Zhou, L.C.; Li, T.K.; Li, H.Y.; Liu, H. WO_3 nanoparticles supported by Nb_2CTx MXene for superior acetone detection under high humidity. *Sens. Actuators B-Chem.* **2024**, *398*, 134710. [CrossRef]
72. Mokoena, T.P.; Swart, H.C.; Hillie, K.T.; Tshabalala, Z.P.; Jozela, M.; Tshilongo, J.; Motaung, D.E. Enhanced propanol gas sensing performance of p-type NiO gas sensor induced by exceptionally large surface area and crystallinity. *Appl. Surf. Sci.* **2022**, *571*, 151121. [CrossRef]
73. Meng, F.; Yang, J.; Wang, Y.-n.; Zhang, R.; Yuan, Z. Acetone gas sensor based on spinel-structured hollow sea urchin-like core–shell ZnO/$ZnFe_2O_4$ spheres. *ACS Appl. Nano Mater.* **2024**, *7*, 16066–16074. [CrossRef]
74. Liang, X.; Fu, S.Y.; Song, X.Y.; Yao, Y.; Gao, N.; Zhang, J. Enhanced acetone gas sensing performance of SnO_2/Zn_2SnO_4 heterojunctions incorporated with MXene: Experimental and theoretical insights. *J. Alloys Compd.* **2025**, *1020*, 179489. [CrossRef]
75. Zhang, Y.; Wang, M.Y.; San, X.G.; Shen, Y.B.; Wang, G.S.; Zhang, L.; Meng, D. $Ti_3C_2T_x$/SnO_2 P-N heterostructure construction boosts room-temperature detecting formaldehyde. *Rare Met.* **2024**, *43*, 267–279. [CrossRef]
76. He, X.X.; Chai, H.F.; Zhou, Y.W.; Liu, K.W.; Yu, Z.X.; Zhang, C. Sensing properties and mechanisms of LaF_3-Co_3O_4 nanorods for low-concentration methanol detection. *Rare Met.* **2024**, *43*, 2193–2204. [CrossRef]
77. Li, L.L.; Diao, Q.; Liu, Z.K.; Zhu, G.X.; Jiao, M.L.; Liu, C.; Du, M.L.; Shi, Y.S.; Wang, Y.L.; Cheng, P.F.; et al. Preparation of Co_3O_4 by tunable oxygen defect engineering and its application in acetone gas sensor. *Microchem. J.* **2025**, *212*, 113481. [CrossRef]
78. Kaixuan, F.; Yun, S.; Lizhe, Y.; Na, J.; Chunfeng, S.; Degang, M.; Xuebin, L.; Rui, H.; Qingling, L. Pt loaded manganese oxide nanoarray-based monolithic catalysts for catalytic oxidation of acetone. *Chem. Eng. J.* **2022**, *432*, 134397. [CrossRef]
79. Zhaoxia, S.; Gongke, L.; Yufei, H. Cataluminescence sensor based on Pt/NU-901 nanocomposite for rapid capture, catalysis and detection of acetone in exhaled breath. *Anal. Chim. Acta* **2022**, *1206*, 339787. [CrossRef]
80. Liu, W.; Xie, Y.L.; Chen, T.X.; Lu, Q.X.; Rehman, S.U.; Zhu, L. Rationally designed mesoporous In_2O_3 nanofibers functionalized Pt catalysts for high-performance acetone gas sensors. *Sens. Actuators B-Chem.* **2019**, *298*, 126871. [CrossRef]
81. Qiu, C.K.; Wang, L.; An, F.; Zhang, H.; Li, Q.R.; Wang, H.Z.; Li, M.J.; Guo, J.Y.; Jia, P.L.; Liu, Z.W.; et al. One-dimensional hollow porous Ru-CuO nanofibers covered with ZIF-71 for H_2S gas sensing and its first-principle study. *Rare Met.* **2025**, *44*, 1170–1181. [CrossRef]
82. Sanam, P.K.J.; Shah, M.D.; Pradyumnan, P.P. Enhanced thermoelectric properties in dual cation doped $CuCrO_2$ nanocrystals mediated by magnon-carrier drag. *Mater. Res. Bull.* **2023**, *164*, 112244. [CrossRef]
83. Zeb, S.; Yang, Z.; Hu, R.M.; Umair, M.; Naz, S.; Cui, Y.; Qin, C.Y.; Liu, T.Y.; Jiang, X.C. Electronic structure and oxygen vacancy tuning of Co & Ni co-doped $W_{18}O_{49}$ nanourchins for efficient TEA gas sensing. *Chem. Eng. J.* **2023**, *465*, 142815. [CrossRef]
84. Li, J.; Zheng, M.; Yang, M.; Zhang, X.F.; Cheng, X.L.; Zhou, X.; Gao, S.; Xu, Y.M.; Huo, L.H. Three-in-one Ni doped porous SnO_2 nanorods sensor: Controllable oxygen vacancies content, surface site activation and low power consumption for highly selective NO_2 monitoring. *Sens. Actuators B-Chem.* **2023**, *382*, 133550. [CrossRef]

Disclaimer/Publisher's Note: The statements, opinions and data contained in all publications are solely those of the individual author(s) and contributor(s) and not of MDPI and/or the editor(s). MDPI and/or the editor(s) disclaim responsibility for any injury to people or property resulting from any ideas, methods, instructions or products referred to in the content.